Computers & Fluids 39 (2010) 345–358

Contents lists available at ScienceDirect

Computers & Fluids

journal homepage: www.elsevier.com/locate/compfluid

MHD flow past a circular cylinder using the immersed boundary method

D.G.E. Grigoriadis [a], I.E. Sarris [b], S.C. Kassinos [a,*]

[a] Computational Science Laboratory UCY-CompSci, Department of Mechanical and Manufacturing Engineering, University of Cyprus, 75 Kallipoleos, Nicosia 1678, Cyprus
[b] Department of Mechanical and Industrial Engineering, University of Thessaly, Athens Avenue, Greece

ARTICLE INFO

Article history:
Received 20 November 2008
Received in revised form 24 July 2009
Accepted 23 September 2009
Available online 29 September 2009

ABSTRACT

The immersed boundary method (IB hereafter) is an efficient numerical methodology for treating purely hydrodynamic flows in geometrically complicated flow-domains. Recently Grigoriadis et als. [1] proposed an extension of the IB method that accounts for electromagnetic effects near non-conducting boundaries in magnetohydrodynamic (MHD) flows. The proposed extension (hereafter called MIB method) integrates naturally within the original IB concept and is suitable for magnetohydrodynamic (MHD) simulations of liquid metal flows. It is based on the proper definition of an externally applied current density field in order to satisfy the Maxwell equations in the presence of arbitrarily-shaped, non-conducting immersed boundaries. The efficiency of the proposed method is achieved by fast direct solutions of the two poisson equations for the hydrodynamic pressure and the electrostatic potential.

The purpose of the present study is to establish the performance of the new MIB method in challenging configurations for which sufficient details are available in the literature. For this purpose, we have considered the classical MHD problem of a conducting fluid that is exposed to an external magnetic field while flowing across a circular cylinder with electrically insulated boundaries. Two- and three-dimensional, steady and unsteady, flow regimes were examined for Reynolds numbers Re_d ranging up to 200 based on the cylinder's diameter. The intensity of the external magnetic field, as characterized by the magnetic interaction parameter N, varied from $N = 0$ for the purely hydrodynamic cases up to $N = 5$ for the MHD cases. For each simulation, a sufficiently fine Cartesian computational mesh was selected to ensure adequate resolution of the thin boundary layers developing due to the magnetic field, the so called Hartmann and sidewall layers. Results for a wide range of flow and magnetic field strength parameters show that the MIB method is capable of accurately reproducing integral parameters, such as the lift and drag coefficients, as well as the geometrical details of the recirculation zones. The results of the present study suggest that the proposed MIB methodology provides a powerful numerical tool for accurate MHD simulations, and that it can extend the applicability of existing Cartesian flow solvers as well as the range of computable MHD flows. Moreover, the new MIB method has been used to carrry out a series of accurate simulations allowing the determination of asymptotic laws for the lift and drag coefficients and the extent of the recirculation length as a function of the amplitude of the magnetic field. These results are reported herein.

1. Introduction

The study of wall bounded MHD flows is a challenging research area with a wide range of applications in engineering and industrial processes. The majority of engineering problems related to liquid metal handling (metallurgical processes, stirring, pumping, casting) involves the interaction of a conducting fluid and an externally applied magnetic field [2]. Other high-impact examples of MHD flows can also be found in cooling circuits of fast fission reactors, or in the self-cooled blankets of fusion reactors, where a liquid metal is used both as coolant and as a breeder material [3]. The addition of Maxwell's laws to ordinary hydrodynamics and the associated action of the Lorentz forces, generate very interesting physical phenomena. In the presence of geometrically complicated boundaries, challenging phenomena may appear, like enhancement or suppression of flow stability [4], induction of secondary flows, modified heat transfer rates [5] etc. A typical example is the use of cylindrical obstacles to induce vortices and enhance heat transfer rates, a concept that has been investigated both experimentally [6–8] and numerically [9–13]. Therefore, the need for accurate and efficient simulations is a key issue in computational magnetohydrodynamics for liquid metals.

Traditionally, the simulation of MHD flows in geometrically complex domains has relied exclusively on unstructured meshes or curvilinear grids [10–13]. On the other hand, for ordinary hydrodynamics in complex domains, an alternative, very economical

* Corresponding author. Tel.: +357 99298621.
E-mail address: kassinos@ucy.ac.cy (S.C. Kassinos).
URL: http://www.ucy-compsci.org (S.C. Kassinos).

0045-7930/$ - see front matter © 2009 Elsevier Ltd. All rights reserved.
doi:10.1016/j.compfluid.2009.09.012

method has been developed, the so called *immersed boundary* (IB) method [14]. In the latter method, a Cartesian mesh solver can be used and discrete momentum forcing is applied in the Navier–Stokes equations to dynamically represent the location and characteristics of the solid boundaries [15–17]. As a result, flows in complicated domains, can be handled with orthogonal, Cartesian grids that may not coincide with solid boundaries.

One of the obvious advantages of the IB method, is the easiness of grid generation. Furthermore, memory and CPU loads are also lower for IB methods compared to boundary fitting curvilinear or unstructured grid methods [18,19]. In cases where the IB method is combined with efficient direct poisson solvers, it reveals its full potential for efficient and accurate simulations in complicated geometries [20]. The same considerations are also very important in MHD simulations, where certain singularities often exist and thin boundary layers have to be resolved [5]. The most difficult flow regions to simulate in wall-bounded MHD flows, are the Hartmann layers, which are formed due to the wall-normal component of the applied magnetic field. The thickness of these Hartmann layers is usually inversely proportional to the intensity of the magnetic field. For this reason, special attention for the proper grid arrangement close to the body has to be paid. The use of the IB method has the potential to simplify the design of grids with adequate resolution in high Hartmann number flows.

Until recently, the IB method had been successfully used only in purely hydrodynamic simulations [17,21,22], and was still waiting for its chance in MHD. The only example of MHD simulations with Cartesian solvers in complex domains, is the recently proposed extension of the immersed boundary method (MIB) for MHD flows [1]. When using the MIB method a properly defined, externally applied current density field is used close to the immersed boundaries in order to satisfy the Maxwell equations and take into account the local electromagnetic conditions, as discussed in detail in [1]. It is important to appreciate that this is the case even in the limit of the quasi-static (QS) approximation that is considered here, where the Lorentz force would normally enter simply as a dummy resistive forcing term in the momentum equations.

Since the MIB method has just been proposed, there is a need for studies that will establish the applicability and accuracy of the method in a range of non-trivial MHD configurations. One such study is the present, where the MHD flow around a circular cylinder is studied in two and three-dimensions. The flow regime in the simulations presented here varies from the steady-state laminar to the periodic or transitional regime. Such a flow is a well-suited test case for validation purposes, because the unsteady nature of the flow leads to interesting flow patterns, including time varying separation points, recirculation regions, shear and boundary layers, etc.

In the following sections, the theoretical formulation is presented first, followed by a discussion of the numerical methodology adopted. A brief review of how the MIB method can be used to account for the electromagnetic part of the calculations is presented next. Finally, computational results and comparisons with previously reported data for the MHD flow around a cylinder are presented and discussed.

2. Theoretical formulation

An incompressible, conductive fluid of density ρ, molecular viscosity μ, dynamic viscosity $\nu = \frac{\mu}{\rho}$ and electric conductivity σ is considered. A uniform stream of fluid with velocity u_∞ flows around a circular cylinder of diameter d as schematically shown in Fig. 1. An external magnetic field of amplitude B_o is applied either along the streamwise direction x, or along the transverse direction z.

In the presence of an externally applied magnetic field, we follow the quasi-static (QS) approximation, which is typically applied

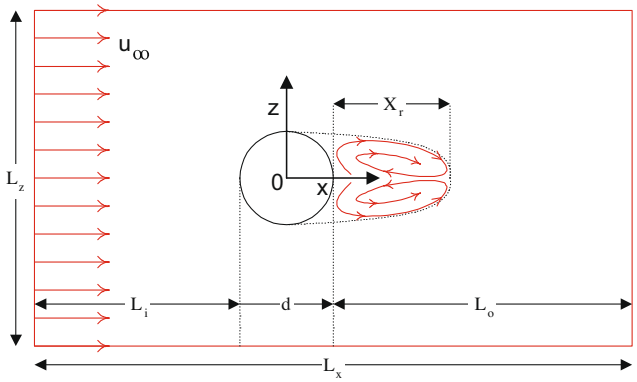

Fig. 1. Computational domain and definition of the main geometrical and flow parameters for the flow over a circular cylinder.

for laboratory scale liquid metal flows. Assuming that the hydrodynamic Re number is significantly larger than unity and that the magnetic Reynolds number $Re_m = \mu^* \sigma u_\infty d$ (where μ^* is the magnetic permeability) is very small, the magnetic diffusion time scale becomes much smaller than the time scale of the flow. Under these conditions, the fluctuations of the magnetic field become much smaller than the applied magnetic field, and the induced currents instantaneously adjust to the velocity fluctuations. Hence, only the external magnetic field enters into the Lorentz force, and one does not have to solve the magnetic induction equations. The flow is completely described by the set of Navier–Stokes equations for an isothermal and conductive incompressible fluid. The continuity and momentum equations can be non-dimensionalized using the cylinder's diameter d and the free stream velocity u_∞ as the characteristic length and velocity scales. In addition, scaling the magnetic field induction by B_o, and the electric field and current density by $u_\infty B_o$ leads to,

$$\nabla \cdot \vec{u} = 0 \tag{1}$$

$$\frac{\partial \vec{u}}{\partial t} + (\vec{u} \cdot \nabla)\vec{u} = -\nabla p + \frac{1}{Re_d}\nabla^2 \vec{u} + N\left(\vec{J} \times \vec{B_o}\right) + \vec{F}_{u,IB}, \tag{2}$$

where the last term $\vec{F}_{u,IB}$, denotes the immersed boundary forcing term for momentum [22], $N(\vec{J} \times \vec{B_o})$ is the Lorentz force $\vec{F_L}$ and $\vec{B_o}$ is the unit vector of the applied magnetic field. Two main dimensionless groups of fundamental importance appear in the equations above, namely the hydrodynamic Reynolds number Re_d and the magnetic interaction parameter N (or Stuart number),

$$Re_d = \frac{u_\infty d}{\nu} \quad \text{and} \quad N = \frac{\sigma B_o^2 d}{\rho u_\infty}, \tag{3}$$

with the latter expressing the ratio of Lorentz forces over inertia forces. In the case of wall-bounded MHD flows, the Reynolds and Stuart numbers can be used to derive the Hartmann number, Ha, which expresses the ratio of Lorentz forces over viscous forces,

$$Ha = \sqrt{Re_d N} = dB_o\sqrt{\frac{\sigma}{\rho \nu}}. \tag{4}$$

The non-dimensional electric current density field $\vec{J}$ of Eq. (2) is governed by Ohm's law according to,

$$\vec{J} = \vec{E} + \vec{u} \times \vec{B_o} + \vec{F}_{j,IB}, \tag{5}$$

where the last term $\vec{F}_{j,IB}$, is the externally imposed current density field associated with the MHD extension of the IB method, which will be discussed in detail in Section (3). The electric field $\vec{E}$ is irrotational and can therefore be expressed in terms of an electrostatic potential as $\vec{E} = -\nabla\Phi$. Since the current density field $\vec{J}$ must also satisfy the charge conservation law, applying the solenoidal

condition $\nabla \cdot \vec{J} = 0$ on Eq. (5), a Poisson's equation can be derived for the electric potential,

$$\nabla^2 \Phi = \nabla \cdot (\vec{u} \times \vec{B_o} + \vec{F}_{j,IB}) = \vec{B_o} \cdot \vec{\omega} + \nabla \cdot \vec{F}_{j,IB}, \tag{6}$$

where $\vec{B_o}$ is the unit vector of the magnetic field direction and $\vec{\omega} = \nabla \times \vec{u}$ is the fluid vorticity. Once the potential field Φ is obtained, the electric current density field $\vec{J}$ can be finally computed from,

$$\vec{J} = -\nabla\Phi + \vec{u} \times \vec{B_o} + \vec{F}_{j,IB}. \tag{7}$$

3. Numerical methodology

Within the quasi-static approach followed in the present study, MHD effects are introduced by the inclusion of the extra Lorentz force term $N(\vec{J} \times \vec{B_o})$ in the momentum Eq. (2). At first glance, it might appear that the computational overhead associated with this term would be small. However, as seen from Eq. (6), the calculation of the current density field involves the solution of an extra Poisson equation for the electric potential at each computational cycle, which serves to enforce the electric charge conservation. It is well known that these poisson solutions are computationally intensive procedures. For example, in a typical hydrodynamic simulation, the pressure solution consumes a major fraction of each computational cycle (usually in the range 30–80%). Thus, for a similar MHD simulation, the inclusion of MHD effects is expected to increase the computational cost significantly (at least by a factor of 1.3–1.8) just due to the required extra solution of the Poisson's equation. Therefore, efficient numerical algorithms for the solution of the Poisson's equation are very important in MHD simulations.

Instead of using expensive iterative solvers, the proposed extension of the IB method uses direct poisson solvers, which are extremely fast, parallel and reliable numerical tools in orthogonal or cylindrical domains [23–25]. Their restrictions in terms of geometrical conformity are completely eliminated by the dynamical representation of solid boundaries. In doing so, MHD flows in complicated, deforming, or even moving boundaries can be simulated using simple Cartesian grids.

The Navier–Stokes equations (2) for a conductive incompressible fluid are solved numerically using the fractional time-step approach [26,20,27] with pressure and electrostatic potential correction. A second-order finite-difference scheme is used for the spatial discretization on orthogonal grids with a staggered variable arrangement. Pressure and electric potential are collocated at the center of each computational cell, while the components of the velocity and the electric current density fields are defined at cell faces. This particular staggered variable arrangement proved to be the most stable and efficient choice for the MIB method, while a collocated variant was found to suffer from spurious oscillations and numerical instabilities [1]. Time advancement is based on a time-splitting, fully explicit, second-order, Adams–Bashforth scheme. The discretised set of Navier–Stokes equations (2) in dimensionless form then read,

$$\frac{\vec{u}|^{n+1} - \vec{u}|^n}{\Delta t} = \frac{3}{2} H(u)|^n - \frac{1}{2} H(u)|^{n-1} - \nabla p|^{n+1}, \tag{8}$$

where exponents denote time level and the operator $H(u)$ contains all the convective, viscous and Lorentz force terms, as well as the momentum IB forcing terms $\vec{F}_{u,IB}$, i.e.,

$$H(u)|^n = -(\vec{u} \cdot \nabla)\vec{u}|^n + \frac{\nabla^2 \vec{u}}{Re_d}|^n + N(\vec{J} \times \vec{B}_o)|^n + \vec{F}_{u,IB}|^n. \tag{9}$$

The calculation of the required current density field $\vec{J}$ from Eq. (7), involves the estimation of the electrostatic potential $\nabla\Phi$. The discretised form of the electric current density field in a domain Ω then becomes,

$$\vec{J}|^n = -\nabla\Phi|^n + (\vec{u} \times \vec{B}_o)|^n + \vec{F}_{j,IB}|^n, \tag{10}$$

which is subject to the charge conservation law $\nabla \cdot \vec{J}|^n = 0$.

The externally imposed immersed boundary current density field $\vec{F}_{j,IB}$ is varying in time and space and should be defined in a consistent way, so that it reflects the type of boundary condition imposed along any existing immersed surfaces Γ_s, in the discrete sense. Thus, the role of $\vec{F}_{j,IB}$, is to drive the current density field and the corresponding electric potential according to the specified boundary conditions imposed along any existing immersed surfaces.

Considering for example a non-conducting, immersed surface, the forcing term $\vec{F}_{j,IB}$ of Eq. (10) should be,

$$\vec{F}_{j,IB}|^n = \begin{cases} +\nabla\Phi|^n - (\vec{u} \times \vec{B}_o)|^n, & \text{along} \Gamma_s \\ 0, & \text{otherwise} \end{cases} \tag{11}$$

so that the proper boundary condition $\vec{J}_\Gamma = 0$ is recovered along a stationary surface Γ_s. However, although the cross product $(\vec{u} \times \vec{B}_o)|^n$ is known, computing the forcing field $\vec{F}_{j,IB}|^n$ of Eq. (11) still requires the estimation of the electric potential $\nabla\Phi|^n$. A possible choice might be the use of Eq. (6) which is usually solved in boundary-conforming MHD simulations without the forcing term $\vec{F}_{j,IB}|^n$. Within the IB method though, setting the forcing term to zero does not provide any means of properly defining the type of internal boundary conditions along the immersed surface. Even more importantly, the charge conservation law would be violated in the vicinity of immersed surfaces. An alternative choice would be to define the unknown forcing term through the application of the solenoidal condition $\nabla \cdot \vec{J}|^n = 0$ in Eq. (10). In that case however, a complicated iterative solution would be required for the Poisson equation of the unknown electric potential (Eq. (6)) since the gradient of the unknown forcing term $\nabla \cdot \vec{F}_{j,IB}|^n$ would appear as a source term.

In order to overcome these difficulties and avoid the use of iterative procedures, a projection scheme for the current density was presented in [1]. In analogy with the immersed boundary methodology for the momentum field, the proposed projection scheme uses a reformulation of Eq. (10) to first define a provisional current density field $\vec{J}|^*$ according to,

$$\vec{J}|^n = \overbrace{-\nabla\Phi|^{n-1} + (\vec{u} \times \vec{B}_o)|^n + \vec{F}_{j,IB}|^n}^{\vec{J}|^*} - \nabla\delta\phi, \tag{12}$$

where $\Phi|^n = \Phi|^{n-1} + \delta\phi$. The provisional field $\vec{J}|^*$ does not satisfy the charge conservation law. Imposing the solenoidal condition on the above equation, to satisfy charge conservation at time level n, leads to a Poisson's equation for the electric potential difference $\delta\phi$,

$$\nabla^2 \delta\phi = \nabla \cdot \vec{J}|^*. \tag{13}$$

Therefore, in this study instead of solving the usual Poisson equation $\nabla^2\Phi = \nabla \cdot (\vec{u} \times \vec{B_o})$, a Poisson equation for the electric *potential difference* $\delta\phi$ is solved (Eq. (13)) using the residuals of the provisional current density field $\vec{J}|^*$ as a source term. Once Eq. (13) is solved, any spurious sources or sinks of electric charge are eliminated and the projections of the electric current density and potential are completed by the following corrections,

$$\vec{J}|^n = \vec{J}|^* - \nabla\delta\phi \tag{14}$$

$$\Phi|^n = \Phi|^{n-1} + \delta\phi. \tag{15}$$

The Poisson's Eq. (13) for the electric potential differences is solved directly, using exactly the same direct poisson solver that is used for the pressure correction. The electric potential Φ is collocated with pressure, while two different variable arrangement schemes

Table 1
Numerical resolution used for the simulation of the two-dimensional flow, for $Re_d \leqslant 150$ (first three from the top), and the three-dimensional flow, for $Re_d = 200$ (last two). The last column refers to the number of nodes used in the area of the cylinder (shown by a dotted line in Fig. 2).

Grid	$n_x \times n_z$	n_y	$\Delta_{x,z,min}$–$\Delta_{x,z,max}$	Δ_y	Resolution in the cylinder area $d \times d$
G1	131×108	–	0.050–0.50	–	20×20
G2	262×216	-	0.025–0.25	–	40×40
G3	450×360	-	0.010–0.10	–	100×100
G1-3	113×96	32	0.050–0.50	0.3125	20×20
G2-3	262×192	64	0.025–0.25	0.1562	40×40

have been tested for the Lorentz forces and current densities. One of the tested schemes is using collocating of variables and the other ordinary staggering. Extensive grid convergence tests on Hartmann flows in ducts have proved that the cell-centered formulation suffers from severe numerical instabilities, while ordinary staggering reached an exceptional agreement with analytical solutions, even with relatively coarse numerical resolutions [1]. Therefore, ordinary staggering is used for all MHD-related variables, and in cases where properties are needed at the cell centers, the consistent interpolation scheme proposed by Ni et al. [28] is used.

The actual calculation of the forcing term $\vec{F}_{j,IB}|^n$ of Eq. (11) is based on interpolation schemes using the current density field of the surrounding fluid nodes, since in the most general case, the immersed boundary interface Γ_s does not always coincide with grid-lines. In the present study, a linear interpolation was used for the forcing nodes, which considers the electric current at the closest boundary point and four of the closest fluid nodes [1]. In this way, the presence of the immersed surface is mimicked dynamically and as it will be shown later, such a current density forcing method can accurately and dynamically mimic the electrostatic definition of any non-conducting immersed surface.

4. Results

The flow over a circular cylinder has been considered in order to demonstrate the capability of the IB method to accurately represent MHD flows in the presence of solid boundaries. The computational domain for the flow considered is shown in Fig. 1.

In the absence of a magnetic field, the flow regime simply depends on the value of the Reynolds number Re_d. It is known that for Reynolds numbers in the range $5 < Re_d < 46$, the flow is in a steady-state and a well-defined, permanent, recirculation pattern of length X_r is formed behind the body. For higher Re_d numbers, the flow starts to develop instabilities at the shear layers forming along the cylinder surface and vortex shedding develops. Under these conditions, the extend of the recirculation region, as well as the drag and lift coefficients, fluctuate periodically in time, with a well-defined frequency. The vortex shedding phenomenon behind the cylinder is characterized by the frequency of vortex generation f, which defines the characteristic Strouhal number for each case,

$$St = \frac{fd}{u_\infty}. \tag{16}$$

Up to $Re_d \approx 188$ the flow is purely 2-D and remains three-dimensionally stable [29]. At higher Re_d values though, 3-D effects appear and the flow develops mode-A and mode-B instabilities at $Re_d \approx 200$ and $Re_d \approx 250$, respectively [29]. Since a 2-D analysis is questionable for $Re_d > 188$, we have performed 2-D computations for Reynolds numbers up to $Re_d = 150$, and 3-D computations for the case of $Re_d = 200$.

The major comparison parameters are the lift and drag coefficients C_l and C_d, as computed from the time evolution of the lift and drag forces F_l and F_d acting on the immersed body, i.e.

$$C_l = \frac{F_l}{\rho u_\infty^2 A_n} \quad \text{and} \quad C_d = \frac{F_d}{\rho u_\infty^2 A_n}, \tag{17}$$

where, A_n is the area normal to the flow direction. These forces have been computed using the reconstruction scheme proposed by Yang

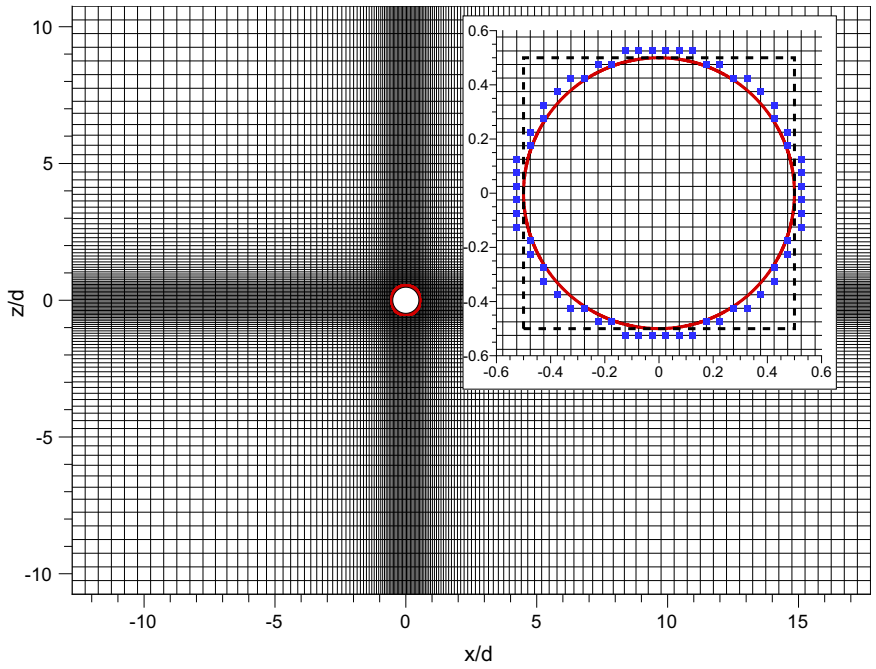

Fig. 2. Computational grid G1 for the simulation of the flow over a circular cylinder and detailed grid distribution in the vicinity of the cylinder. The full symbols correspond to the locations of the *forcing nodes* [1,21] where direct forcing is imposed (see Section 3). The numerical resolution used in the area of the cylinder (dotted line) is given in Table 1 for each grid.

and Balaras [21], which is suitable for IB methods. The time variation of the lift coefficient C_l has been used to estimate the frequency of the vortex generation and the corresponding Strouhal number, as well as the flow regime (steady or unsteady).

In the following paragraphs, the purely hydrodynamic cases are presented first, followed by the MHD cases for streamwise and transverse magnetic fields.

4.1. Computational parameters

A circular cylinder of diameter d is located at a distance of $L_i = 12d$ from the inlet of the domain, while the outlet is located at $L_o = 17d$ behind the body. Along the transverse, z-direction, the cylinder is symmetrically placed along the centerline with the domain extending to $L_z = 21d$. In doing so, a blockage ratio of $d/L_z < 5\%$ is established so that possible end-effects on the vortex shedding mechanism are minimized [30].

Along the surface of the immersed cylinder, a non-slip wall boundary condition is used. At the inlet of the domain, a constant velocity profile is imposed, while convective outflow conditions [31] are specified for the outlet. Along the z-direction, Neumann and Dirichlet boundary conditions have been applied for the streamwise and transverse velocity components u and w, respectively, i.e.,

$$\left.\frac{\partial u}{\partial z}\right|_{z=0,L_z} = 0 \quad \text{and} \quad w|_{z=0,L_z} = 0. \tag{18}$$

For the 3-D calculations, a slightly smaller computational domain is used, with the cylinder located at a distance of $L_i = 7d$ from the domain's inlet, and the outlet located at $L_o = 13d$ behind the body. In the transverse direction, the cylinder was symmetrically located along the centerline with the domain extending to $L_z = 16d$. Along the axis of cylinder in the spanwise direction, the total size of the domain extended to $L_y = 12d$. The boundary conditions used were identical with those of the 2-D cases described above and symmetry boundary conditions have been applied along the lateral direction, y. Table 1 summarizes the grid configurations used for the 2-D and the 3-D simulations of the present study. Grid stretching has been applied in the x and z-directions, and close to the cylinder surface a uniform grid has been used of equal spacing in the x and z-directions as shown in Fig. 2.

Within the quasi-static approach adopted here, a variable time step is used for the calculations, which is dynamically adjusted according to the convective (CFL) and viscous time scale (VSL) criteria: $CFL < 0.2$ and $VSL < 0.05$. The total computational overhead associated with the MHD solution (solving the Poisson's equation, computing currents with MIB method, including forces etc.) was thus of the order of 80%. From this computational overhead, less than 5% is devoted to the MIB method. For more details on the MIB method and its implementation, the reader can consult Ref. [1]. Due to the efficiency of the direct poisson solver used, the resulting computer code has excellent parallel efficiency and re-

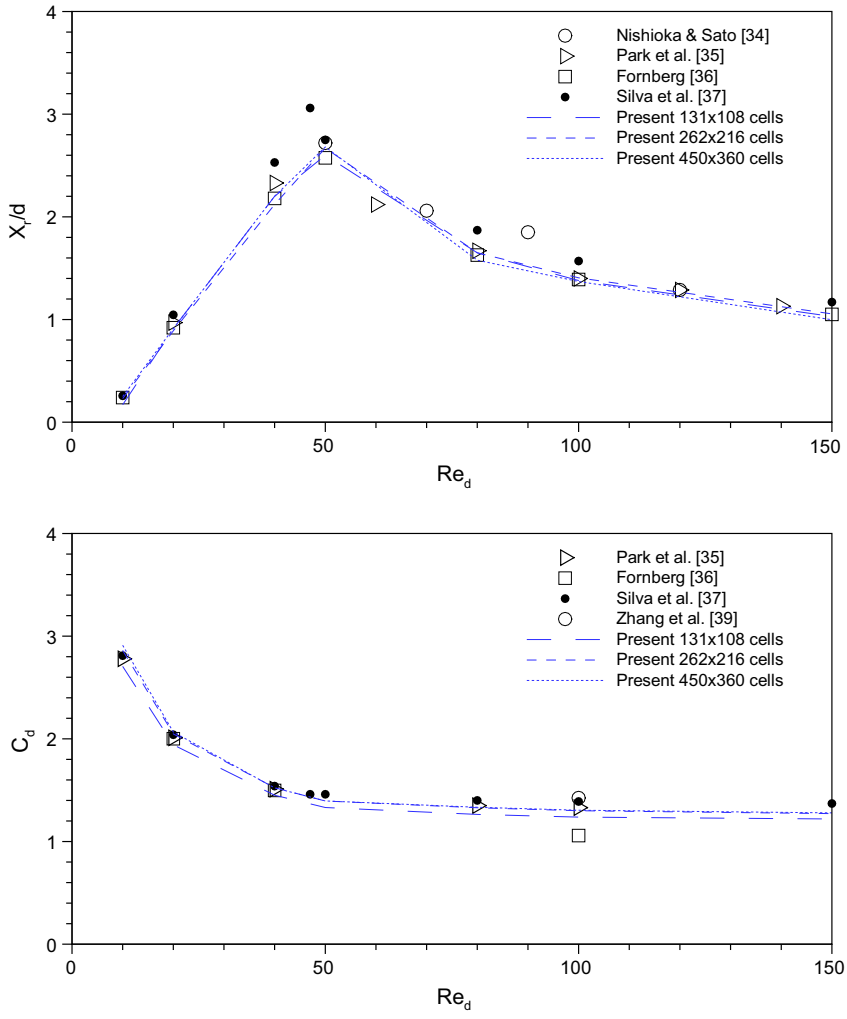

Fig. 3. Normalized length of recirculation region after the cylinder, X_r/d (upper) and drag coefficient C_d (bottom) for the purely hydrodynamic case as compared with previous experimental [34,39] and numerical [35–37] studies.

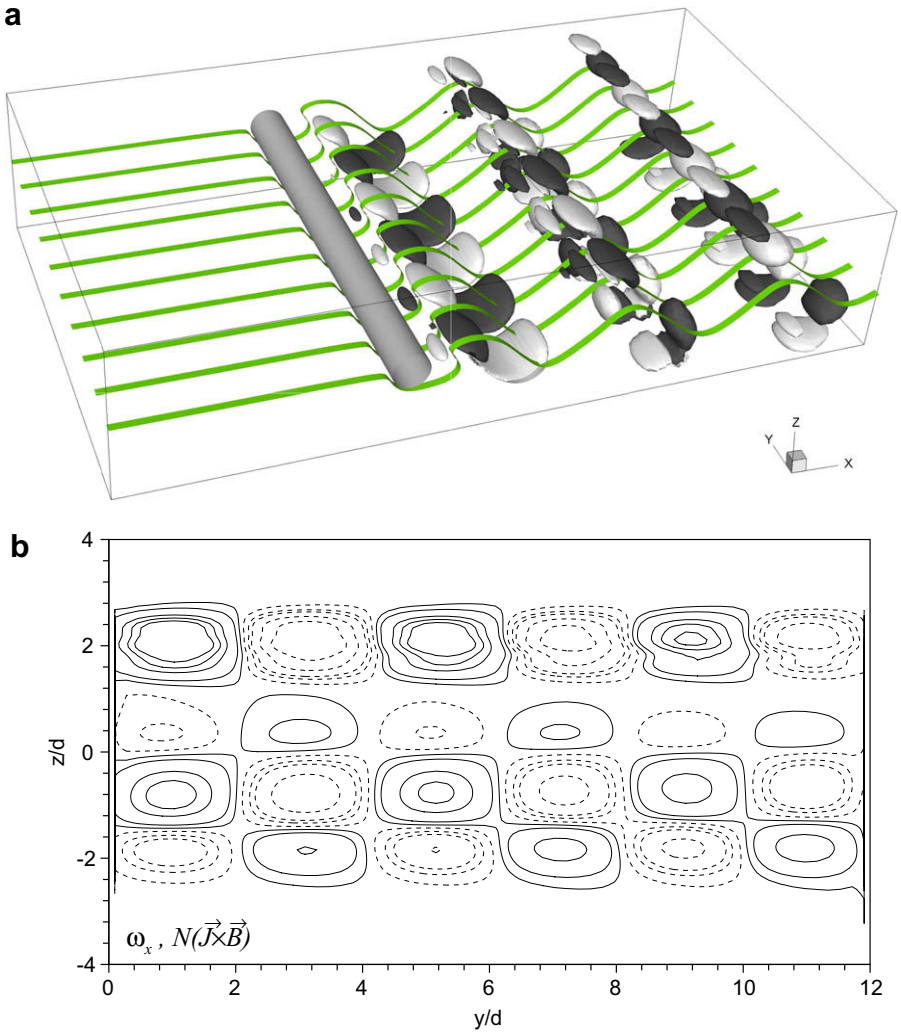

Fig. 4. Instantaneous streamwise vorticity for $Re_d = 200$, (a) dark and light surfaces correspond to $\omega_x = 0.0004$ and $\omega_x = -0.0004$, respectively, (b) streamwise vorticity ω_x at $x/d = 13$ (dashed lines correspond to negative values of $\omega_x = \left(\frac{\partial w}{\partial y} - \frac{\partial v}{\partial z}\right)$).

Table 2
Predicted values of the mean lift and drag coefficients and Strouhal number for $Re_d = 200$.

Case, (grid)	$\overline{C_d}$	C_l'	St
Present (G1-3)	1.29	0.53	0.205
Present (G2-3)	1.30	0.60	0.204
Zhang et al. [39]	1.29	0.53	0.201
Mutschke et al. [29]	1.30	0.60	0.197

quires a limited amount of physical memory (135 Mb per million nodes). For a fully 3-D calculation, performances of 0.28 μs/node/timestep and 0.52 μs/node/timestep were reached for a hydrodynamic and a full MHD problem respectively (on Dual AMD@2.6 GHz processors).

A similar, purely hydrodynamic flow configuration was tested with an in-house developed flow-solver based on a the methodology described in [32]. Using a body-fitted approach, this solver required more than five times the amount of physical memory and was 10–40 times slower to execute in terms of μs/node/timestep on the same computational resources. Similar numbers were obtained for the serial speedup and the memory efficiency when the present implementation was compared to other body-fitted flow solvers as those reported in [33] for the benchmark case of the 3-D flow around a circular cylinder.

4.2. 2-D and 3-D purely hydrodynamic cases for $10 \leqslant Re_d \leqslant 200$

Fig. 3 shows the variation of the computed mean recirculation length, X_r, and drag coefficient, C_d, as a function of the Reynolds number in the range $20 \leqslant Re_d \leqslant 150$. A very good agreement with previous numerical and experimental studies [34,35] is achieved, even for the lower numerical resolutions used. Furthermore, present results agree very well with the numerical results reported in [36] for the hydrodynamic case. The same applies for the comparison against the numerical study of Lima-E-Silva et al. [37], who had also used the IB method and found good agreement with the statistics reported in older numerical or experimental studies.

Figs. 4a and b show the 3-D mode-A instability [38] for the higher Reynolds number case ($Re_d = 200$), as computed using the finer grid G2-3. Starting from an arbitrary initial field, a periodic three-dimensional flow develops. This is indicated by the deformation of the primary vortex in the cylinder's wake and by the formation of vortex pairs as shown in Fig. 4b. The wavelength of these structures along the axis of the cylinder was found to be $\lambda_y \approx 4.0d$, in agreement with the value of $\lambda_y \approx 4d$ reported in [39] for a similar configuration. Table 2 shows the mean lift and drag coefficients as well as the Strouhal number for the $Re_d = 200$ case and for the grids used in the 3-D simulations. The comparison against the results of Refs. [29,39] shows an excellent agreement.

Table 3
Subset of the examined cases for the magnetohydrodynamic flow over a circular cylinder at $Re_d = 100$. Predicted force statistics and time averaged recirculation length compared with reference values, using different numerical resolutions.

Case, grid	N_x	N_z	$\overline{C_d}$	X_r
G1	0.5	–	1.12	2.50
G2	0.5	–	1.19	2.50
G3	0.5	–	1.21	2.52
Mutschke et al. [12]	0.5	–	–	2.4
G1	1.0	–	1.26	1.85
G2	1.0	–	1.33	1.84
G3	1.0	–	1.40	1.85
Mutschke et al. [12]	1.0	–	–	1.8
G1	5.0	–	1.95	1.59
G2	5.0	–	2.06	1.56
G3	5.0	–	2.06	1.56
Mutschke et al. [12]	5.0	–	–	1.49
G1	–	0.08	1.41	1.72
G2	–	0.08	1.48	1.77
G3	–	0.08	1.53	1.77
Mutschke et al. [12]	–	0.08	–	1.78
G1	–	0.5	2.72	0.26
G2	–	0.5	2.78	0.29
G3	–	0.5	2.82	0.29
Mutschke et al. [12]	–	0.5	–	0.30
G1	–	1.0	4.03	0.00
G2	–	1.0	4.09	0.00
G3	–	1.0	4.12	0.01
Mutschke et al. [12]	–	1.0	–	0.00

4.3. 2-D magnetohydrodynamic cases for $10 \leqslant Re_d \leqslant 150$

Once the numerical methodology was verified for the hydrodynamic calculations, as described in the previous section, a series of 2-D MHD cases were computed. In these simulations, the hydrodynamic field was used as an initial condition and the magnetic field was switched on after several characteristic time units.

Two different directions of the magnetic field have been considered, with the interaction parameter denoted as N_x or N_z for a streamwise or a transverse magnetic field, respectively. For a 2-D flow along the x–z plane, following Eqs. (2) and (5) one can easily show that,

$$\begin{aligned} &\text{streamwise field } B_x \neq 0, \vec{J} = (0, wB_x, 0), \vec{F_L} = (0, 0, -N_x w B_x^2) \\ &\text{transverse field } B_z \neq 0 \vec{J} = (0, -uB_z, 0), \vec{F_L} = (-N_z u B_z^2, 0, 0) \end{aligned} \tag{19}$$

As a consequence of Eq. (6), the electrostatic potential Φ and the electric field $\vec{E}$ become zero for both of these cases. The produced current density $\vec{J} = \vec{u} \times \vec{B}$ was taken into account although it lied along the cylinder axis. As it can also be seen from Eq. (19), the Lorentz forces modify the vorticity field by acting on the transverse and streamwise components of the velocity field with intensity $-N_x w B_x^2$ and $-N_z u B_z^2$ for a streamwise or a transverse magnetic field, respectively.

Simulations were performed for different values of the interaction parameter in order to investigate the effect of the magnetic field on the flow patterns, the flow regime and the lift and drag coefficients C_l and C_d.

Table 3 presents a subset of the computed cases and the predicted parameter values for the MHD cases at $Re_d = 100$. A satisfactory agreement is evident between different numerical resolutions, even for the higher values of the interaction parameter N, where the resolution of the Hartmann layers becomes marginal. Using lower numerical resolutions led to a slight underestimation of drag coefficient values, while the extend of the recirculation zone and the time evolution of the force coefficients remained identical for all practical purposes. Therefore, most of the 2-D results presented below are based on the lower numerical resolution of 131×108 cells.

4.3.1. Effect on lift coefficient C_l and flow steadiness

The degree of modification of the flow field by the action of the Lorentz forces becomes stronger as the amplitude of the magnetic field is increased, independently of its direction. The Lorentz forces oppose the vortical motion and eventually suppress the vortex shedding mechanism. Therefore, for both magnetic field directions, the amplitude of the lift coefficient C_l is reduced monotonically until the flow becomes completely steady. This is clearly demonstrated in Fig. 5, where the time variation of the lift coefficient for $Re_d = 100$ is shown for the cases of a streamwise and a transverse magnetic field. Depending on the magnetic field amplitude, the flow either remains unsteady (for weak magnetic fields) or becomes completely steady above a critical value of the interaction parameter.

The highest values of interaction parameters for which the unsteady periodic regime was preserved were found to be $N_x = 0.14$ and $N_z = 0.07$. On the other hand, a steady flow was obtained for $N_x = 0.16$ and $N_z = 0.09$. Therefore, the critical values for the transition from the periodic unsteady regime to the steady flow regime for the present study were $N_{x,CR} = 0.15$ and $N_{z,CR} = 0.08$, i.e. in good agreement with the values of $N_{x,CR} = 0.14$ and $N_{z,CR} = 0.10$ reported in [12].

Upon the activation of the magnetic field, the amplitude of the sinusoidal lift coefficient variation undergoes an exponential reduction with time. The time-response of the flow to the activation of the Lorentz forces was found to depend both on the flow regime and the magnetic field strength. For weak magnetic fields and unsteady cases ($N_x < N_{x,CR}$, or $N_z < N_{z,CR}$), the time needed for the transition to the new state of the flow was found to increase with the interaction parameter. For instance the flow responds in a couple of shedding cycles for the case of $N_x = 0.025$ (Fig. 5a), while more than 10 shedding cycles were required before the lift coefficient reached the new equilibrium value for the case of $N_x = 0.1$ (Fig. 5b). Once periodic vortex shedding is eliminated in the steady flow regime, the flow responds faster to the Lorentz forces as the magnetic field intensity is increased.

For all cases examined, it is found that, at a constant value of the interaction parameter, a transverse magnetic field is much more effective in damping the flow unsteadiness than a magnetic field along the steamwise direction. As mentioned in Section 4.3, this can be explained by the fact that for the 2-D cases considered, a transverse magnetic field generates streamwise Lorentz forces proportional to the local streamwise velocity component u. In the case of a streamwise magnetic field, the Lorentz forces act on the transverse component of momentum, being proportional to the local transverse velocity component w.

The evolution of the lift coefficients seemed overall to be relatively insensitive to the orientation of the magnetic field, with similar trends being observed for both the streamwise and transverse magnetic fields. For both cases, the amplitude of the lift coefficient was reduced monotonically with the interaction parameter, while the Strouhal number was found to decrease with the magnetic field intensity for a streamwise field and increase slightly for a transverse magnetic field.

4.3.2. Effect on drag coefficient C_d and recirculation

In contrast with the lift coefficient, the evolution of the drag coefficient C_d, is more sensitive to the orientation of the magnetic field as shown in Fig. 6. It is interesting to note that for a streamwise magnetic field, and for values of the interaction parameter in the range $N_{x,CR} < N_x < 0.9$, the values of the drag coefficient remain below the hydrodynamic value at the same Re number. Within that range, C_d shows a non-monotonic behavior with respect to the magnetic field strength.

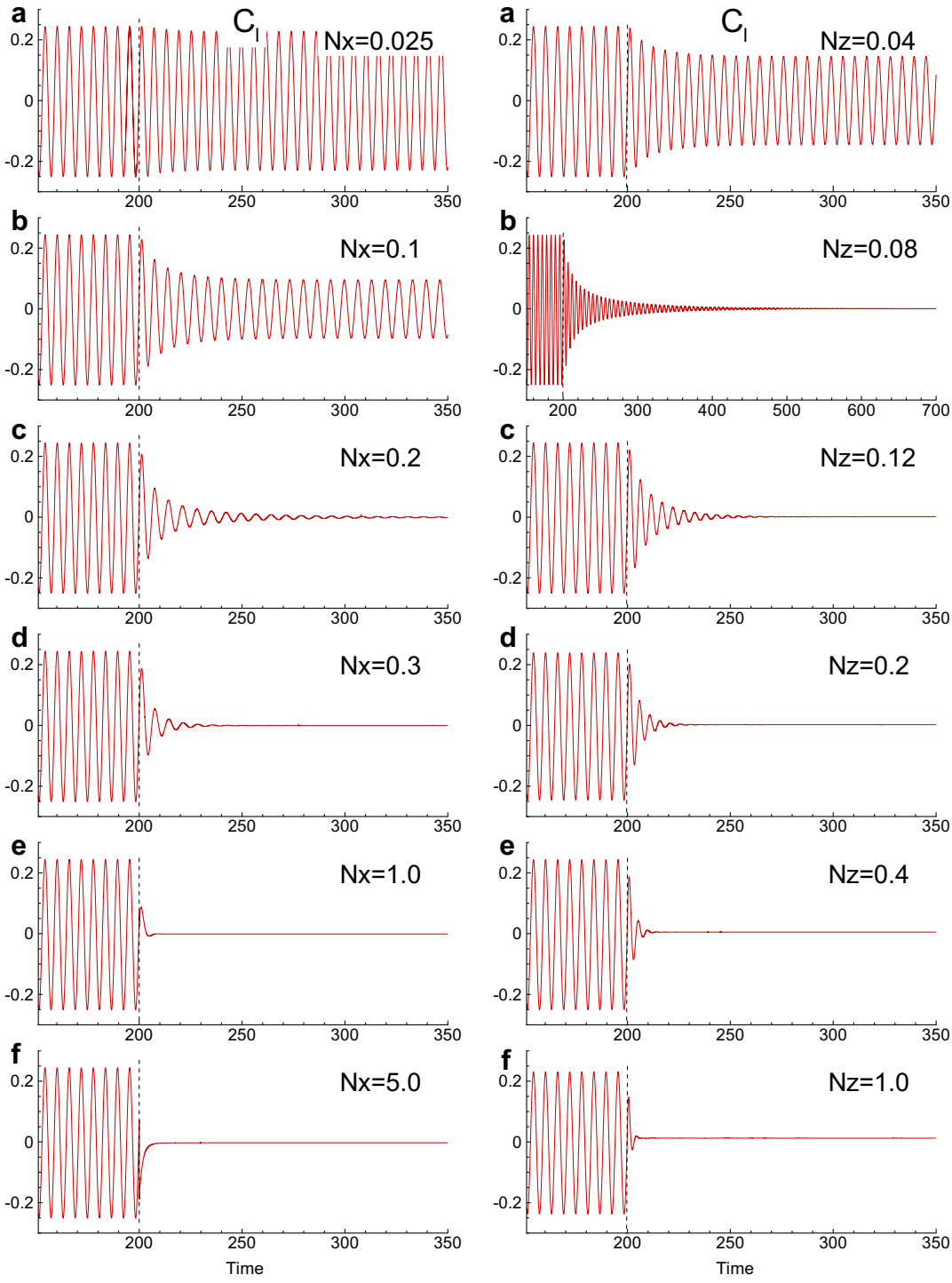

Fig. 5. 2-D magnetohydrodynamic flow at $Re_d = 100$. Effect of the magnetic field strength on the time evolution of the lift coefficient C_l for a streamwise (left) and a transverse magnetic field (right). The dotted line denotes the activation of the magnetic field at $t = 200$.

For weak streamwise magnetic fields, (i.e. $N_x < N_{x,CR} = 0.15$), drag reduces linearly with N_x down to 22% of its hydrodynamic value. Within this range, the shear stress forces were found to decrease monotonically with N_x (even for higher values of N_x up to $N_x < 5$). Therefore, the observed drag reduction for weak magnetic fields, was due to the distribution of the pressure forces around the cylinder. Although both upstream and downstream base pressure levels were higher than the hydrodynamic values, the downstream base pressure recovered faster in the range $N_x < 0.15$, leading to reduced drag coefficients.

In this unsteady flow regime region, the inertia forces dominate and the action of the Lorentz force $-N_x w B_x^2$ weakly opposes the transverse velocity component w. This leads to a narrower vortex street behind the body, and therefore to longer mean recirculation regions with respect to the hydrodynamic case. It is interesting to note that at the threshold of the unsteady flow regime, the mean recirculation length X_r is increased by a factor of 2.6 with respect to the hydrodynamic case (Fig. 7).

For stronger streamwise magnetic fields $N > N_{x,CR}$, the damping action of the Lorentz forces dominates and eventually eliminates

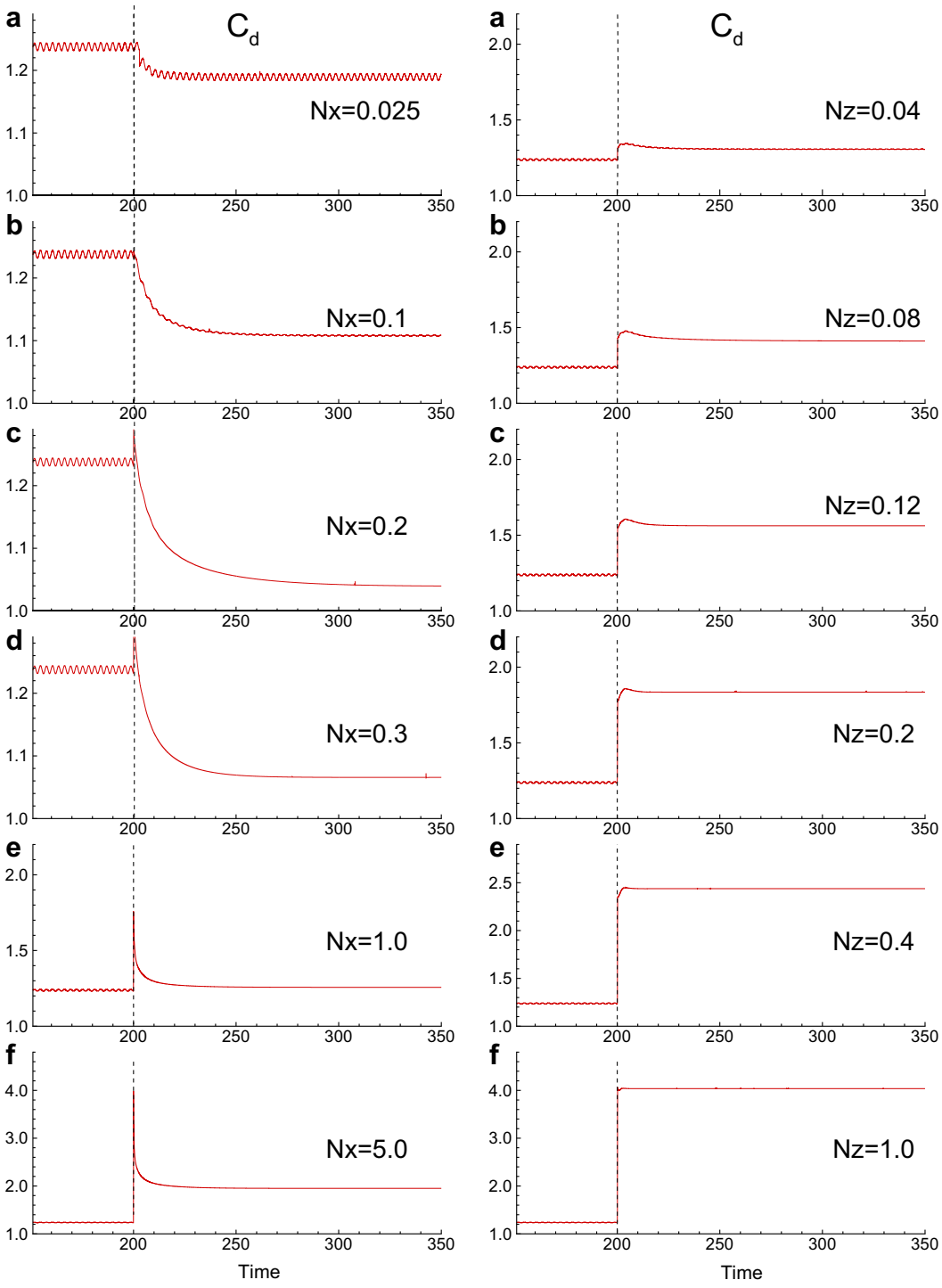

Fig. 6. 2-D magnetohydrodynamic flow at $Re_d = 100$. Effect of the magnetic field strength on the time evolution of the drag coefficient C_d for a streamwise (left) and a transverse magnetic field (right). The dotted line denotes the activation of the magnetic field at $t = 200$.

vortex shedding. In this regime, the downstream pressure drops significantly, while the upstream one keeps increasing, leading to ever increasing values of the drag coefficients in the form $C_d \propto \sqrt{N_x + c}$. The recirculation length follows an exponential decay in the form $X_r \propto (e^{-N_x+c}) + C_{X_r}$, reaching asymptotically the value of $C_{X_r} \simeq 1.53d$ for $N_x = 2.0$. For stronger streamwise magnetic fields, the recirculation is not reduced further due to the existence of a very slow-moving region formed before the body (Fig. 8) known as "upstream wake" [12].

Such a non-monotonic behavior for the drag coefficient is only experienced in the case of a streamwise magnetic field. For the case of a transverse magnetic field, the Lorentz forces are acting directly to dump the mainstream velocity component. Therefore, an increase in the magnetic field strength was always associated with an increased difference between upstream and downstream pressures and led to increased drag coefficients (Fig. 7) in the form $C_d \propto (N_z + c)^k + C_{C_d}$. Non-monotonic behavior at small interaction parameters is observed only in the extent of the recirculation zone

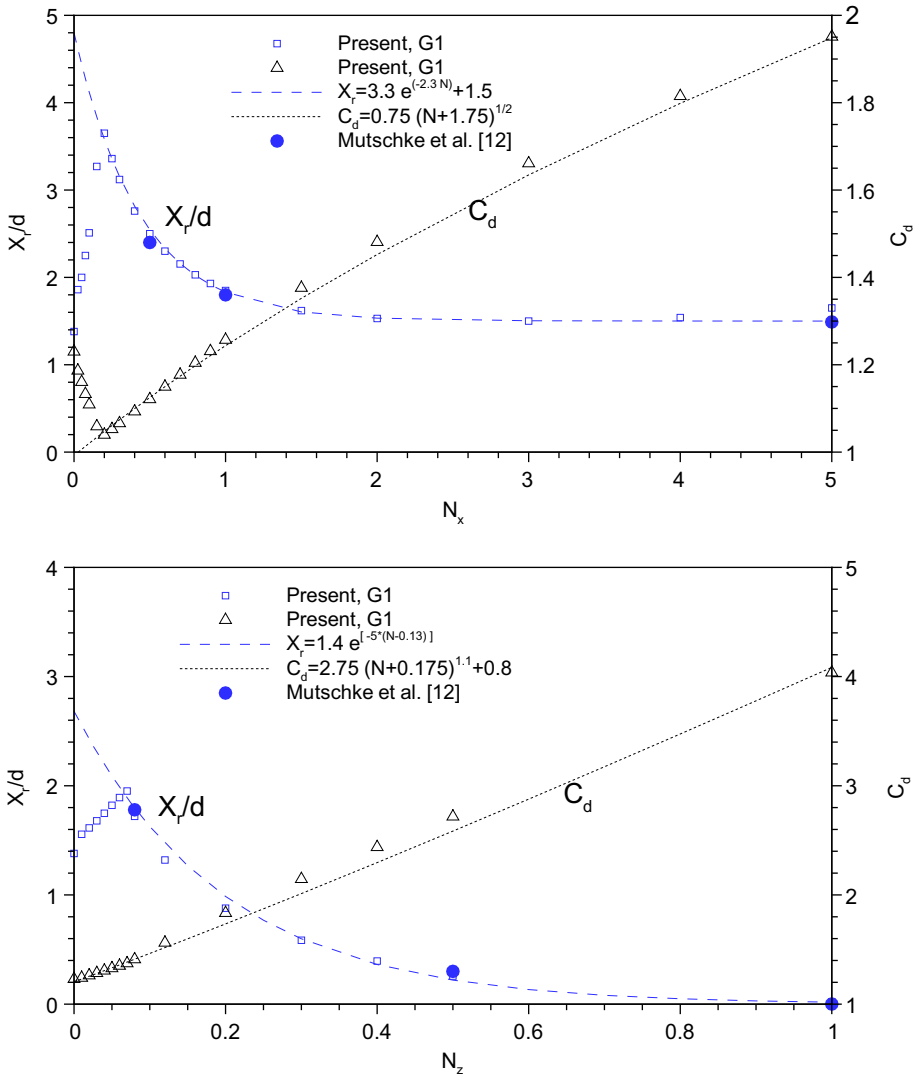

Fig. 7. Effect of streamwise (top) and transverse (bottom) magnetic field intensity N_x, N_z on drag coefficient C_d and mean recirculation length X_r for $Re_d = 100$.

X_r, and only for $N_z < 0.08$, due to the transition to the steady flow regime. In contrast to the streamwise magnetic field case, for a transverse magnetic field, recirculation is clearly diminished for the higher values of the interaction parameter examined. For $N_z > 0.08$, X_r drops exponentially to zero with increasing N_z in the form $X_r \propto (e^{-N_z+c})$. The mean location of flow separation is also severely affected by the magnetic field. As shown in Fig. 8, separation occurs earlier and separation points move upstream as the intensity of the magnetic field is increased [12,8]. For higher values of the magnetic field, though, the separation points recover slightly, in line with previous studies [29].

4.4. 3-D magnetohydrodynamic case for $Re_d = 200$

For the purely 2-D flow cases with electrically insulating boundaries presented in Section 4.3, the electrostatic potential Φ and the electric field $\vec{E}$ do not contribute to the computed current density $\vec{J}$. Therefore, in order to fully validate the MIB methodology for the estimation of the electric field $\vec{E}$, but also to demonstrate its potential, a fully 3-D case at $Re_d = 200$ was also considered with a streamwise magnetic field. Such a case was selected because of the presence of instabilities and the existence of the spanwise velocity v, which generates streamwise vorticity ω_x (see Fig. 4). Under these conditions, the electric field is activated because the electric potential, Φ, is driven by the source term ω_x (Eq. 6). The results of these 3-D simulations are presented next.

Fig. 10a shows a snapshot of the electric field potential Φ and the current density vector field $\vec{J}$ for the 3-D MHD simulation computed with the MIB method. These snapshots were taken at the midplane along the spanwise direction y. The potential field lines close to the cylinder surface clearly show the ability of the MIB method to properly resolve the electric field. The actual Lorentz force exerted on the fluid is shown in Fig. 10b and d, where the damping effect of the magnetic field on the transverse velocity component w and the spanwise vorticity ω_y are clearly demonstrated. The transverse velocity leads to opposing Lorentz forces suppressing the vortex-shedding mechanism and narrowing the wake [9]. Additionally, the streamwise vorticity, ω_x, which contributes to three-dimensionality and mode-A instability, is suppressed by the action of opposing vorticity as shown in Fig. 11.

The dependence of the computed lift and drag coefficients, and of the recirculation zone length, on the magnetic field intensity is shown in Fig. 9. A good agreement is noted with the reference data of Mutschke et al. [29] using different numerical resolutions. The difference for the recirculation length and the drag coefficient were found on the average to be less than 1% and 3% for both grids, while the largest discrepancies ($\approx$11%) were noticed for the rms value C_l' when using the coarser grid resolution at the unsteady flow

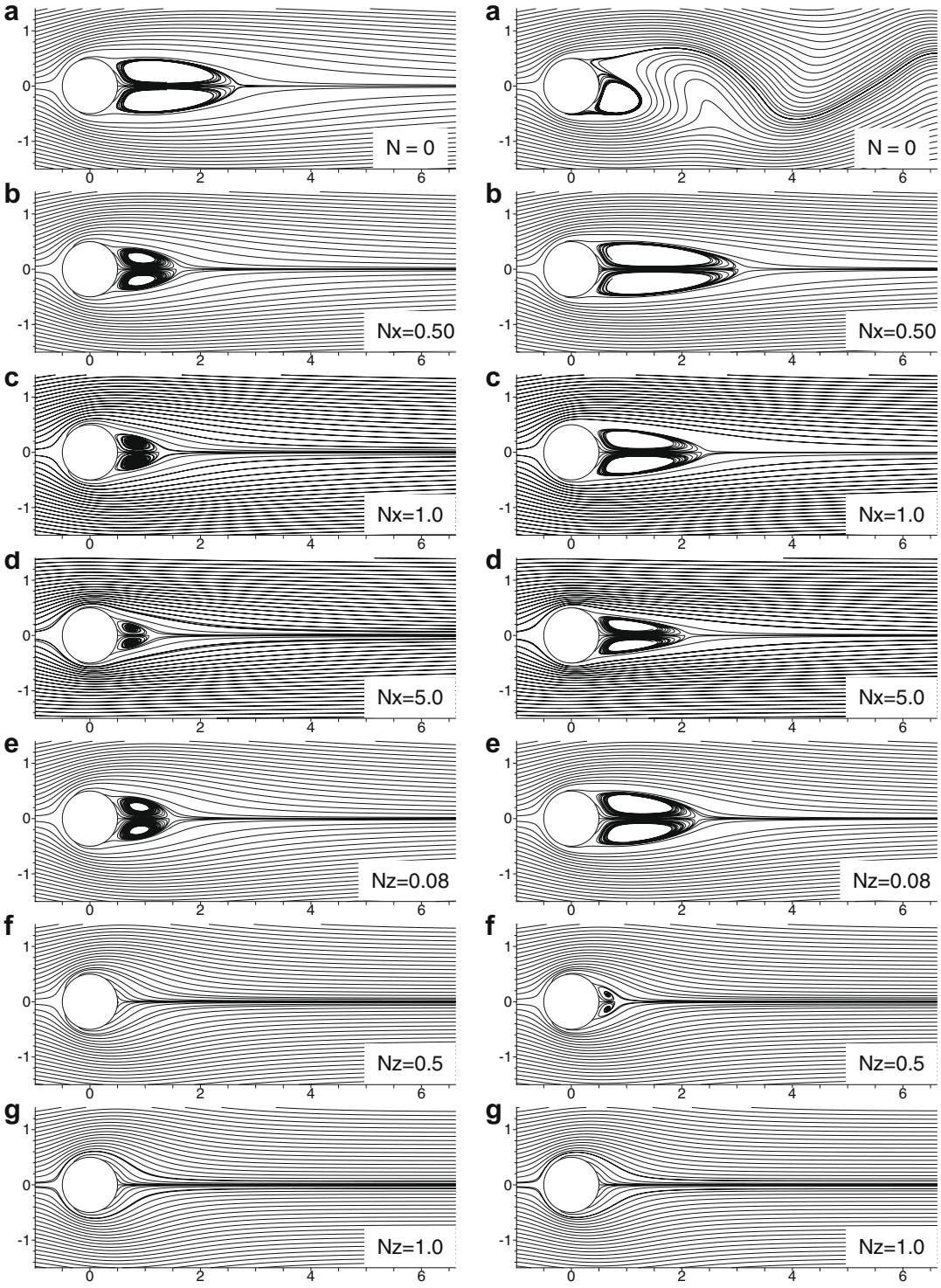

Fig. 8. Instantaneous recirculation patterns for the flow over the cylinder at $Re_d = 40$ (left) and $Re_d = 100$ (right). (a) Purely hydrodynamic case, (b–d) streamwise magnetic field at $N_x = (0.5, 1.0, 5.0)$, (e–g) transverse magnetic field at $N_z = (0.08, 0.5, 1.0)$.

regime. In line with the 2-D case presented earlier, as the magnetic field strength is increased, the amplitude of the lift force decays, and the drag coefficient drops until the three dimensionality of the flow is fully suppressed. Transition to a purely 2-D flow was found to take place for interaction parameter values in the range $0.3 < N_x < 0.4$ as in the study of Mutschke et al. [29]. As in the 2-D cases, a further increase of the magnetic field strength leads to a monotonic increase of the drag coefficient.

5. Conclusions

The recently proposed MIB method is a natural extension of the immersed boundary method for MHD simulations in complicated geometries, using direct solution for both the pressure and the electrostatic potential on cartesian grids. The objective of this study was to investigate the performance of the MIB method and to demonstrate its potential for the computation of MHD flows in

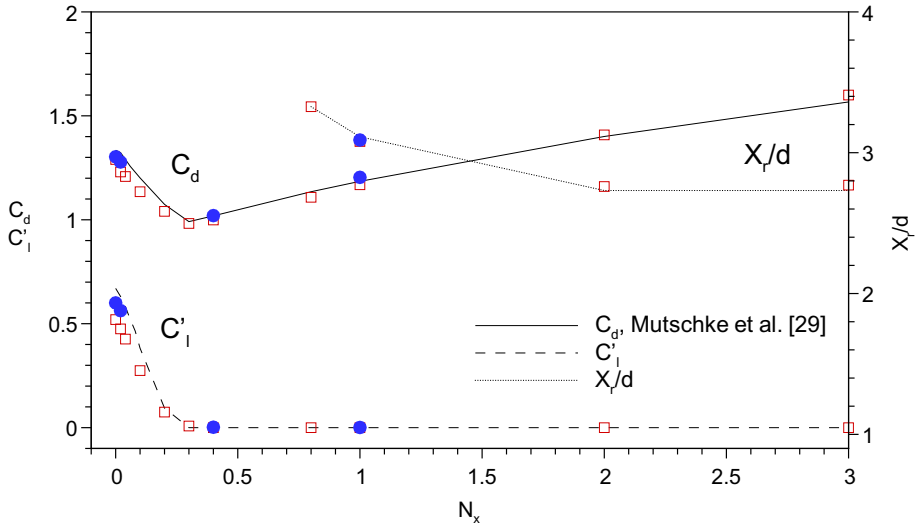

Fig. 9. Effect of streamwise magnetic field intensity N_x on the mean value of the drag coefficient C_d, the rms value of the lift coefficient C_l' and the recirculation length X_r for the 3-D cases at $Re_d = 200$. Open symbols: grid G1-3, closed symbols: grid G2-3, lines: Mutschke et al. [29]

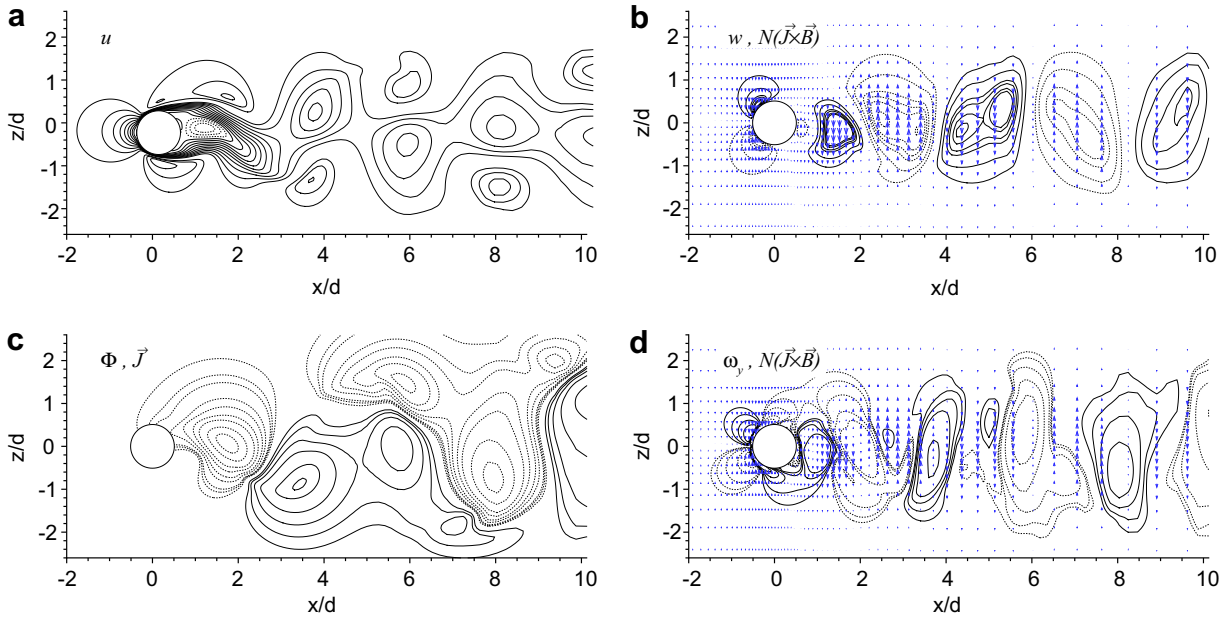

Fig. 10. Damping effect of Lorentz forces for the 3D MHD flow at $Re_d = 200$ at the midplane at $y = 6d$. Instantaneous snapshot 0.04 time units after the application of a streamwise magnetic field with $N_x = 0.02$. (a) Contour lines of streamwise velocity component u, (b) contour lines of transverse velocity component w and vector field of the Lorentz force $N_x(\vec{J} \times \vec{B})$, (c) distribution of electric potential Φ, vector field of magnetic current density $\vec{J}$, (d) contour lines of spanwise vorticity ω_y, vector field of the Lorentz force $N(\vec{J} \times \vec{B})$ (every fourth point shown here, dotted lines indicate negative values).

complex geometries. For this purpose, the flow of a conducting fluid past a circular cylinder under a streamwise or a transverse magnetic field was computed. Two-dimensional and three-dimensional simulations for the steady and unsteady flow regimes around a circular cylinder were conducted.

For the case of a streamwise magnetic field, a non-monotonic variation of the drag coefficient and recirculation length was found in both the 2-D and 3-D cases. As a result, for a wide range of interaction parameters, the drag coefficient was found smaller than the corresponding hydrodynamic value. Comparison of the present results for the critical interaction parameters, the drag and lift coefficients, the recirculation length and the Strouhal number showed very good agreement with published results. Thus, we can conclude that the MIB method is very efficient, even in the presence of flow instabilities. The application to turbulent flows and more complex geometries is under development.

Since our results are consistent with the theory of the fluid flow past the circular cylinder, we use them to produce asymptotic relations for variation of the studied quantities as a function of the magnetic field amplitude. In the steady flow regime, the value of the drag coefficient was found to vary according to $\sqrt{N_x + c}$, and of the recirculation region length according to e^{-cN_x}, reaching a plateau value for the higher magnetic field amplitudes. The reversal of stability order has also been verified from the 3-D cases in accordance with previously reported data [29]. In cases with a transverse magnetic field, the damping effect on the vortex street was found to be stronger, and a non-monotonic behavior was noticed only for the recirculation length.

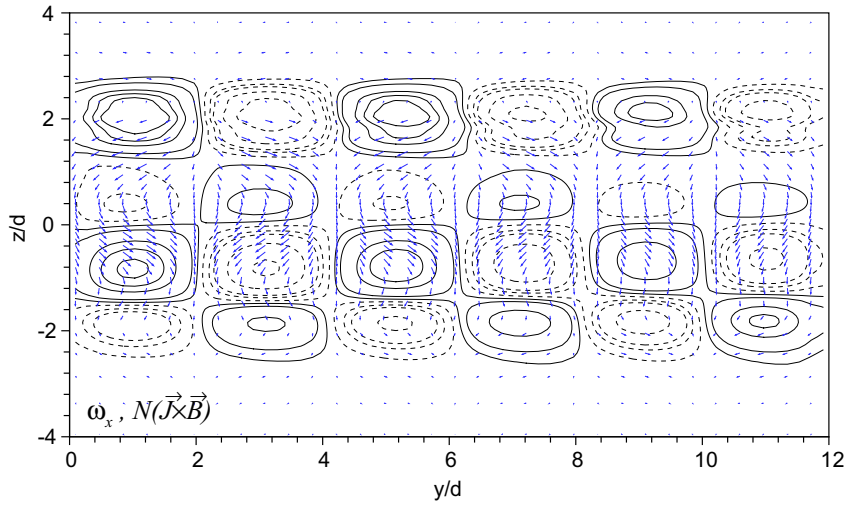

Fig. 11. Instantaneous streamwise vorticity ω_x for $Re_d = 200$ at $x/d = 13$, after the application of a streamwise magnetic field with $N_x = 0.02$ (also see Fig. 4). The vector field corresponds to the Lorentz forces, and dashed lines to negative values of $\omega_x = \left(\frac{\partial w}{\partial y} - \frac{\partial v}{\partial z}\right)$.

The values of drag coefficient vary almost linearly according to $(N_x + c)^{1.1}$.

Acknowledgments

E. Balaras is greatly acknowledged for providing help on the implementation of the IB method. This work has been performed under the UCY-CompSci project, a Marie Curie Transfer of Knowledge (TOK-DEV) grant (contract No. MTKD-CT-2004-014199) funded by the CEC (under the 6th Framework Program) and the contract of association ERB 5005 CT 99 0100 between the European Atomic Energy Community and the Hellenic Republic. A first draft of the present manuscript was written when IES was a EURATOM fellow at Université Libre de Bruxelles, Belgium, under an intra-European fellowship (contract No 016818). Partial support by a Center of Excellence grant from the Norwegian Research Council to Center for Biomedical Computing is also greatly acknowledged.

References

[1] Grigoriadis DGE, Kassinos CS, Votyakov EV. Immersed boundary method for MHD flows of liquid metals. J Comput Phys 2009(3):903–20.
[2] Davidson PA. An introduction to magnetohydrodynamics. Cambridge texts in applied mathematics. Cambridge University press; 2001.
[3] Morley NB, Smolentsev S, Barleon L, Kirillov IR, Takahashi M. Liquid magnetohydrodynamics – resent progress and future direction for fusion. Fusion Eng Des 2000;51–52:701–13.
[4] Müller U, Bühler L. Magnetohydrodynamics in channels and containers. Springer; 2001.
[5] Moreau R. Magnetohydrodynamics. Kluwer Academic Publishers.; 1990.
[6] Papailiou DD. Magneto-fluid-mechanic turbulent vortex streets. In: Fourth Beer-Sheva seminar on MHD flows and turbulence. AIAA; 1984. p. 152–73.
[7] Kolesnikov Y, Tsinober A. Experimental investigation of two-dimensional turbulence behind a grid. Fluid Dyn 1974;9:621–4.
[8] Lahjomri J, Caperan P, Alemany A. The cylinder wake in a magnetic field aligned with the velocity. J Fluid Mech 1993;253:421–48.
[9] Mück B, Günther C, Müller U, Bühler L. Three-dimensional MHD flows in rectangular ducts with internal obstacles. J Fluid Mech 2000;418:265–95.
[10] Mutschke G, Gerbeth G, Shatrov V, Tomboulides A. Two and three-dimensional instabilities of the cylinder wake in an aligned magnetic field. Phys Fluids 1997;9:3114–6.
[11] Sekhar TVS, Sivakumar R, Kumar H, Ravi kumar TVR. Effect of aligned magnetic field on the steady viscous flow past a circular cylinder. Appl Math Model 2007;31:130–9.
[12] Mutschke G, Shatrov V, Gerbeth G. Cylinder wake control by magnetic fields in liquid metal flows. Exp Thermal Fluid Sci 1998;16:92–9.
[13] Dousset V, Pothérat A. Numerical simulations of a cylinder wake under a strong axial magnetic field. Phys Fluids 2008;20:017104.
[14] Peskin CS. Flow patterns around heart valves: a numerical method. J Comput Phys 1972;10:252–71.
[15] Fadlun EA, Verzicco R, Orlandi P, Mohd-Yusof J. Combined immersed boundary finite-difference methods for three-dimensional complex simulations. J Comput Phys 2000;161(2):35–60.
[16] Lai MC, Peskin CS. An immersed boundary method with formal second-order accuracy and reduced numerical viscosity. J Comput Phys 2000;160:705–19.
[17] Verzicco R, Orlandi P, Mohd-Yusof J, Haworth D. LES in complex geometries using boundary body forces. AIAA J 2000;38:427–33.
[18] Kim J, Kim D, Choi H. An immersed-boundary finite-volume method for simulations of flow in complex geometries. J Comput Phys 2001;171:132–50.
[19] Mohd-Yusof J. Development of immersed boundary methods for complex geometries. Annu Res Briefs 1998:325–36 [Center for turbulence research].
[20] Grigoriadis DGE, Bartzis JG, Goulas A. LES of the flow past a rectangular cylinder using the immersed boundary concept. Int J Num Meth Fluids 2003;41:615–32.
[21] Yang J, Balaras E. An embedded-boundary formulation for large-eddy simulation of turbulent flows interacting with moving boundaries. J Comput Phys 2006;215(1):12–40.
[22] Balaras E. Modeling complex boundaries using an external force field on fixed Cartesian grids in large-eddy simulations. Comput Fluids 2003;33:375–404.
[23] Schumann U. A direct method for the solution of Poisson's equation with Neumann boundary conditions on a staggered grid of arbitrary size. J Comput Phys 1976;20:171–82.
[24] Swarztrauber PN. The methods of cyclic reduction, Fourier analysis and the FACR algorithm for the discrete solution of Poisson's equation on a rectangle. J Comput Phys 1977;19:490–501.
[25] Wilhelmson RB, Ericksen JH. Direct solutions for Poisson's equation in three dimensions. J Comput Phys 1977;25:319–31.
[26] Kim J, Moin P. Application of a fractional-step method to incompressible Navier–Stokes equations. J Comput Phys 1985;59:308–23.
[27] Grigoriadis DGE, Bartzis JG, Goulas A. Efficient treatment of complex geometries for large-eddy simulations of turbulent flows. Comput Fluids 2004;33:201–22.
[28] Ni M-J, Munipalli R, Morley NB, Huang P, Abdou MA. A current density conservative scheme for incompressible MHD flows at a low magnetic Reynolds number. Part I: on a rectangular collocated grid system. J Comput Phys 2007;227(1):174–204.
[29] Mutschke G, Gerbeth G, Shatrov V, Tomboulides A. The scenario of three-dimensional instabilities of the cylinder wake in an external magnetic field: a linear stability analysis. Phys Fluids 2001;13(3):723–34.
[30] Zdravkovich MM. Flow around circular cylinders. Applications, vol. II. Oxford Science Publ.; 2003.
[31] Pauley LL, Moin P, Reynolds WC. A numerical study of unsteady laminar boundary layer separation. TF-34, thermoscience division. Stanford University: Dept. of Mech. Eng.; 1988.
[32] Ham F, Mattsson K, Iaccarino G. Accurate and stable finite volume operators for unstructured flow solvers. Annu Res Briefs. Stanford University: Center for Turbulence Research; 2006. p. 243–61.
[33] Turek S. Recent benchmark computations of laminar flow around a cylinder. In: Proc 3rd world conference in applied computational fluid mechanics, freiburg; 1996. http://citeseer.ist.psu.edu/article/turek96recent.html.
[34] Nishioka M, Sato H. Mechanism of determination of the shedding frequency of vortices behind a cylinder at low Reynolds numbers. J Fluid Mech 1978;89:49–60.
[35] Park J, Kwon K, Choi H. Numerical solutions of flow past a circular cylinder at Reynolds number up to 160. KSME Int J 1998;12:1200.

[36] Fornberg B. A numerical study of steady viscous flow past a circular cylinder. J Fluid Mech 1980;98:819–55.
[37] Lima-E-Silva ALF, Silveira-Neto A, Damasceno JJR. Numerical simulation of two-dimensional flows over a circular cylinder using the immersed boundary method. J Comput Phys 2003;189:351–70.
[38] Williamson HK. Vortex dynamics in the cylinder wake. J Fluid Mech 1996;328:345–539.
[39] Zhang HQ, Fey U, Noack BR, König M, Eckelmann H. On the transition of the cylinder wake. Phys Fluids 2001;7(4):779–94.